Batteries & Supercaps

Research Article
doi.org/10.1002/batt.202400697

Chemistry Europe
European Chemical Societies Publishing

www.batteries-supercaps.org

Unraveling the Degradation Mechanism of $LiNbO_3$-Coated NCM Cathode at High Potential in All-Solid-State Batteries Using 10 K Extended X-ray Absorption Fine Structure Analysis

Yong Jun Park,[a] Yixiao Su,[a] Kentaro Yamamoto,[b] Toshiki Watanabe,*[a] Neha Thakur,[a] Mukesh Kumar,[a] Toshiyuki Matsunaga,[a] and Yoshiharu Uchimoto[a]

All solid-state batteries (ASSBs) utilizing sulfide-based solid electrolytes hold promise for enhancing battery energy density while mitigating safety concerns, thus meeting the stringent requirements for electric vehicle applications. For the practical application of ASSBs, it is important to stabilize the interface between the solid electrolyte and the cathode. Although cathode coated with a thin layer of $LiNbO_3$ provide higher interface stability, which significantly improves charge-discharge and cycle performance, degradation at high potentials has also been noted. In this study, we focused on the degradation mechanism of $LiNbO_3$-coated $LiNi_{0.5}Co_{0.2}Mn_{0.3}O_2$ cathode active materials at high potentials by using three electrode system for ASSBs, which allows separating the impedance measurement of the interface between cathode and solid electrolyte. We performed X-ray absorption spectroscopy (XAS) measurements at low temperature (10 K) to analyze the local structure around Nb and correlate these findings with impedance measurements. Our results indicate that the impedance of $LiNbO_3$ increased rapidly due to the oxygen desorption reaction at high potentials. This study aims to elucidate the dynamic changes and degradation mechanism of $LiNbO_3$-coated $LiNi_{0.5}Co_{0.2}Mn_{0.3}O_2$ in ASSBs and provide new ideas for the design of interfacial coating materials.

Introduction

The need for batteries with safe and high energy density, driven by the rapid adoption of electric vehicles, is driving the desire to commercialize all-solid-state batteries (ASSBs) with solid electrolytes (SEs) as a replacement to the traditional lithium-ion batteries (LIBs) with liquid electrolytes. Over the past decades, significant progress has been made in the study of several solid electrolytes, including sulfide,[1,2] oxide,[3,4] and polymer solid electrolytes.[5] Among them, sulfide solid electrolytes are considered as the most promising candidates for commercialization of ASSBs due to their excellent lithium-ion conductivity (ranging from 10^{-4} to 10^{-2} S cm^{-1}), and good formability.[6] Besides solid electrolytes with high ionic conductivity, lithium metal anodes and high voltage cathode active materials are necessary to realize practical ASSBs with high energy density. However, in ASSBs, advances in electrochemical performance are hampered by inadequate ion channel connectivity stemming from the nature of solid and limited contact area between the active material and solid electrolyte particles.[7] This challenge is particularly pronounced in composite electrodes, where the electrochemical behavior is strongly influenced by the microstructure and the interface between the electrode and the electrolyte.[8,9] Therefore, understanding and managing the formation and evolution of the interface during battery assembly and cycling is essential to all-solid-state battery performance.[10]

Despite the development of sulfide solid electrolytes with high ionic conductivities comparable to those of liquid electrolytes,[1] the practical application of ASSBs has been hampered by the low air stability of sulfide solid electrolytes and the issues of chemical and electrochemical stability at the electrode/electrolyte interface.[11,12] Specifically, the interface challenges between these electrolytes and the cathode encompass various issues, including the creation of interfacial space charge layer, elemental interdiffusion at the interface, oxidative decomposition of sulfide electrolytes under high voltages, and stress generation during charge and discharge cycles.[13,14] Especially due to the relatively narrow electrochemical stability window of sulfide SEs, pairing them with high-voltage cathode materials like layered oxides (e.g., $LiCoO_2$, $LiNi_{1-x-y}Co_xMn_yO_2$) results in considerable interfacial impedance, primarily attributed to suboptimal interface compatibility.[13] In detail, sulfide electrolytes tend to undergo oxidative decomposition above 2.1 V (vs. Li^+/Li), corresponding to the S^0/S^{2-} redox couple. This decomposition reaction generates by-products with low ionic conductivity, such as S and P_2S_5, at the interface.[15] Conse-

[a] Y. J. Park, Y. Su, T. Watanabe, N. Thakur, M. Kumar, T. Matsunaga, Y. Uchimoto
Graduate School of Human and Environmental Studies,
Kyoto University,
Yoshida-nihonmatsu-cho, Sakyo-ku,
Kyoto 606-8501, Japan
E-mail: watanabe.toshiki.7z@kyoto-u.ac.jp

[b] K. Yamamoto
Faculty of Engineering,
Nara Women's University,
Kitauoya-nishimachi,
Nara 630-8263, Japan

Supporting information for this article is available on the WWW under https://doi.org/10.1002/batt.202400697

quently, the direct interaction between sulfide electrolytes and oxide cathodes, particularly at high voltages during charging, leads to oxidative decomposition and the creation of a high-impedance interfacial layer.[15]

To address these interfacial challenges, surface coatings on cathode active materials have been employed to enhance the stability of the electrode/SE interface.[16,17] Coating materials such as $LiNbO_3$,[18] $Li_4Ti_5O_{12}$,[19] $LiTaO_3$,[20] Li_2SiO_3,[21] and Li_3PO_4[22] have been utilized for surface coating of cathode active materials. Among them, $LiNbO_3$ has been widely utilized due to its ease of application and high ionic conductivity, especially in the amorphous state,[23] and offers improved charge-discharge performance and cyclic stability.[24,25] However, the upper limit of the electrochemical stability window of $LiNbO_3$ is only 3.7 V (vs. Li^+/Li), which is lower than the cutoff voltage of high-voltage cathodes such as $LiCoO_2$ and $LiNi_{(1-x-y)}Co_xMn_yO_2$.[26] This results in the degradation of $LiNbO_3$ coating material under high cutoff potentials, which limits the commercial viability of $LiNbO_3$ as a coating material for cathode active materials.[27,28]

Kobayashi et al.[27] reported that in high voltage charging and discharging cycles involving a Li_2S–P_2S_5/$LiNbO_3$ coated $LiNi_{0.33}Co_{0.33}Mn_{0.33}O_2$ (NCM333) cathode, a small amount of PO_x formed on the outer surface of the $LiNbO_3$ coating. Nevertheless, they noted the absence of oxygen release from the surface of NCM333 beneath the Li_2S–P_2S_5/$LiNbO_3$ coating. Morino et al.[28] observed that cathode active materials maintained about 80% capacity retention after approximately one month of floating test in harsh conditions at 4.55 V (vs. Li^+/Li) and 60 °C. However, the results of time-of-flight secondary ion mass spectrometry (ToF-SIMS) and X-ray photoelectron spectroscopy (XPS) indicated that oxidative decomposition of the sulfide solid electrolyte was evident. Further analysis indicated that the $LiNi_{0.5}Co_{0.2}Mn_{0.3}O_2$ region remained unchanged before and after the test, suggesting that the oxidation did not originate from the cathode active material itself, but from the $LiNbO_3$ coating material. These findings highlight the need for a deeper understanding of the degradation mechanisms of $LiNbO_3$ under high-voltage conditions.

In this research, we concentrate on $LiNbO_3$, widely used as cathode coating material, within the context of composite cathode with sulfide solid electrolyte. We successfully isolated polarization effects during cycling by incorporating a home-made reference electrode to establish a three-electrode system in the ASSB. This approach enabled us to separately investigate the degradation reactions at the cathode side and the associated changes in interfacial impedance. Additionally, we employed synchrotron radiation X-ray absorption spectroscopy (XAS) at extremely low temperature of 10 K to analyze the potential dependence of the local structure of $LiNbO_3$. This analysis successfully suppresses the signals from the thermal disorder to enable a quantitative examination of the correlation between various potentials and local structural transformations, shedding light on the high-potential degradation mechanism of $LiNbO_3$. The comprehensive results from these investigations are intended to elucidate the functional mechanism and dynamic evolution of new interfacial coating layers in ASSBs, thus offering novel insights and methodologies for the design of efficient interfacial coatings.

Experimental Section

Material Preparation

A $LiNbO_3$–coated $LiNi_{0.5}Co_{0.2}Mn_{0.3}O_2$ ($LiNbO_3$–coated NCM, 1 wt%,) was obtained from Sumitomo Metal Mining, Japan. Coating of $LiNbO_3$ onto the surface of $LiNi_{0.5}Co_{0.2}Mn_{0.3}O_2$ (NCM) particles is done using the following methods described in the previous reports.[25,29] 0.21 mol of Li metal was dissolved in 685.2 g of anhydrous ethanol and mixed with 0.21 mol of niobium pentaethoxide under Ar atmosphere. The solution was sprayed onto the NCM particles with a spraying rate of 2 g/min by using rolling fluidized coating machine (MP-01, Powrex). After coating, annealing at 400 °C for 30 minutes under an oxygen flow was conducted. The composite cathode was prepared by hand mixing of $LiNbO_3$–coated NCM and $Li_{7-x}PS_{6-x}Cl_x$ (x~1, LPSCl, D_{50} = 3.5 μm, Mitsui Mining & Smelting Co., Ltd.) in weight ratio of 70:30 in an agate mortar for 30 minutes.

Chemically reduced $Li_4Ti_5O_{12}$(R-LTO) was prepared as per the methodology outlined in the reference.[30] In detail, naphthalene lithium was synthesized by mixing 6 mmol of metallic lithium (Honjo Metal Co., Ltd., thickness of 0.25 mm) and 6 mmol of naphthalene (Sigma-Aldrich, 99%) in 30 mL of tetrahydrofuran (Fujifilm Wako Co., Ltd.), followed by stirring for 24 hours. Then, 3 mmol of $Li_4Ti_5O_{12}$ (Toshima Co., Ltd., 99%) was introduced to the solution and stirred for 1 hour, leading to a formation of 2 mmol of $Li_7Ti_5O_{12}$. The solution was filtered to obtain deep blue powder, and the filtered powder was dried under vacuum for 24 hours. The dried powder was heated at 441 K for 1 hour. All procedures above were done in an argon-filled glove box (Miwa Manufacturing Co., Ltd., MDB-1.5KP-UH7).

The R-LTO reference electrode was prepared by manual applying of R-LTO onto a nickel mesh current collector (3Ni7-3/0, Taiyo Wire Cloth, aperture ratio: 90–91%, thickness of 0.08 mm). First, blending of the R-LTO powder with polyvinylidene fluoride (PVDF) (Fujifilm Wako Co., Ltd.) in a weight ratio of 6.4:1 in N-methyl-2-pyrrolidone (Fujifilm Wako Co., Ltd.) was processed in a blender at 2000 rpm for 2 minutes. The resultant paste was then uniformly spread onto the nickel current collector and dried at 353 K for 24 hours in an oven. The R-LTO composite material's mass loading on the current collector was approximately 7 mg cm^{-2}. To ensure the reference electrode's functionality, no SE or conductive additive was included in the R-LTO reference electrode formulation.

Characterization

X-ray diffraction (XRD) measurements were performed utilizing the RINT-Ultima III (Rigaku) instrument, equipped with CuKα radiation at a wavelength of 1.54056 Å and operating at 40 kV and 40 mA, and beamline BL02B2 in SPring-8. The analysis encompassed a 2θ range from 10° to 80° with scan speed of 2°/min and sampling interval of 0.02° for all materials. Samples containing sulfide SE were prepared in an argon gas environment within a glovebox. Post-preparation, these samples were secured in a sample holder, designed to protect the samples from exposure to oxygen during the measurement. For the measurement process in SPring-8, the wavelength was set to 0.41491 Å utilizing a Si (111) double crystal spectrometer, and calibration was carried out with cerium oxide (CeO_2). Moreover, Rietveld analysis of the acquired XRD pattern was conducted using Jana 2006 software, enabling the identification of

the crystal structure. Transmission electron microscopy (TEM) images were obtained by utilizing JEM-2100F (JEOL, Japan) operated at 200 kV with EDS accessory of JED-2300T (JEOL, Japan). X-ray computed tomography (CT) was utilized to investigate the morphology of $LiNbO_3$–coated NCM composite cathode and conducted at beamline BL20XU at SPring-8 with an X-ray energy of 30 keV.

The Nb K-edge of *ex-situ* XAS spectra of the pellets of composite cathodes in a pristine state underwent 12 hours of maintaining different cut-off potentials (4.0, 4.2, 4.4, 4.6, and 4.8 V vs. Li^+/Li) and underwent charging at 4.8 V (vs. Li^+/Li) for various charging times (0, 1, 4, 8, and 12 h) were measured using the fluorescence yield method at beamline BL14B2 at SPring-8. In addition, samples with different hours (0, 1, 4, and 8 h) of maintaining cut-off potentials of 4.8 V (vs. Li^+/Li) were also prepared and measured at BL14B2. The obtained data were normalized, and then the background was processed and fitted using Athena and Artemis software[31] to obtain the structural parameters of the samples. The XAS measurement was performed at an ultra-low temperature of 10 K to suppress the Debye-Waller factor, thereby reducing noise signals and enhancing the overall quality of the data.

For the S and P K-edge of *ex-situ* XAS spectra of the LPSCl SE after 12 hours of different potential maintenance, it was performed at BL6N1 at the Aichi synchrotron optical center, and K_2SO_4 and Li_3PO_4 were used for energy calibration. All obtained data were normalized and processed by Athena. The measurement sample was prepared according to the following procedures. A double-sided carbon tape was pasted on the sample holder, and samples were pasted onto the carbon tape in a glove box with an Ar atmosphere. By fixing the sample holder with the sample on it to a sample rack, placing it in a transfer vessel, and then sealing it, measurements can be taken without reacting with moisture or oxygen in the atmosphere.

Electrochemical Measurements

Li-In | LPSCl | NCM cells were constructed for electrochemical testing in a glove box filled with argon. To ascertain the influence of the R-LTO reference electrode on the cell's electrochemical performance and during electrochemical impedance spectroscopy (EIS), experiments were conducted using a three-electrode cell configuration, as depicted in Figure S1a. To verify the platform voltage of R-LTO, coin cells were assembled specifically for the test.

An all-solid-state three-electrode cell was prepared in a polyether ether ketone (PEEK) tube (φ10 mm) by cold-pressing LPSCl with chrome-plated SUS current collectors at 360 MPa followed by cold-pressing of 10 mg of $LiNbO_3$-coated NCM composite cathode powder on the one side of LPSCl pellet. Then, Li-In electrode was made on the other side by cold-pressing Li foil (Honjo Metal Co., Ltd., thickness of 0.25 mm) and In foil (Nilaco Co., Ltd., thickness of 0.3 mm) at 160 MPa. In detail, for the three-electrode cell, the R-LTO reference electrode was located in LPSCl powder layers between the NCM electrode and the Li-In electrode. The electrical contact to the reference electrode was achieved by the Ni wire passed through the pinhole on the PEEK tube (Figure S1b and Figure S1c). The masses of the LPSCl powder layers were 80 mg and 120 mg for the NCM electrode side and the Li-In electrode side, respectively. For two-electrode cell, the R-LTO reference electrode is no longer inserted into the LPSCl layer, and the mass of the LPSCl is reduced to 80 mg.

The coin cell consists of the R-LTO electrodes, a polypropylene separator, a lithium metal electrode with a thickness of 0.2 mm, and an electrolyte of 1 M $LiPF_6$ in EC/DMC (volume ratio: 3:7). The R-LTO electrodes were prepared by mixing 80 wt% R-LTO powders, 10 wt% of the conductive acetylene black (Denka Co., Japan) as a conductor, and 10 wt% PVDF as a binder, within a 1-methyl-2-pyrrolidinone solvent. And the thickness of R-LTO electrodes was contained to 30 μm using a doctor blade.

Galvanostatic cycling tests were carried out using a multichannel electrochemical system (SD-8, Hokuto Denko Co., Ltd.) The full cells were subjected to galvanostatic cycling experiments at different current densities at 25 °C with a cut-off voltage of 2.0 V–3.6 V (cell voltage). For the coin cells, galvanostatic cycling experiments were conducted at 25 °C with a cut-off voltage of 1.2 V–3.5 V (vs Li^+/Li). The applied current rate was 10 mA g^{-1}.

The EIS of $LiNbO_3$-coated NCM cathode side were measured using ModuLab ECS (Solartron) at 25 °C by utilizing three-electrode configuration, amplitude 10 mV, and frequency range from 1 MHz to 0.1 Hz. The EIS of the full cell, cathode side and anode side were measured to check the three-electrode cell configuration's applicability to separate each impedance component. Among them, the full cell impedance is obtained by two-electrode cell, while the impedance of the cathode side and anode side are obtained by three-electrode cell. In a glove box filled with argon, after assembling the cell according to the aforementioned process, three impedances were measured initially and after full charging at 0.1 C (1 C = 160 mA g^{-1}). All the samples for measuring the impedance of cathode were first fully charged with the multichannel electrochemical system to different cut-off potentials (4.0, 4.2, 4.4, 4.6 and 4.8 V, vs. Li^+/Li) at 0.1 C, and then maintained at the corresponding potentials for 12 hours, and the impedance of cathode was measured every hour. Ultimately, utilizing ZView software (Ametek Science Instruments) for curve fitting, we calculated the values of each resistance component and their corresponding capacitance from the obtained Nyquist plots.

Results and Discussion

First of all, the XRD pattern of the $LiNbO_3$-coated NCM and its Rietveld refinement result are shown in Figure 1a. The Rietveld refinement analysis reveals that $LiNbO_3$-coated NCM is consistent with a layered hexagonal α-$NaFeO_2$ type crystal structure, space group $R\bar{3}m$, with a = 2.8704 Å and c = 14.2376 Å. For $LiNbO_3$, due to the minimal $LiNbO_3$ content coated on the surface of NCM, which is approximately 2 nm thick, as depicted in Figure 1b, the signal intensity for XRD testing is too low to be effectively measured is consistent with the previous study.[32] Given the inability to detect the $LiNbO_3$ coating signal on the NCM surface through XRD characterization, the surface morphology of the $LiNbO_3$-coated NCM particles was examined by the TEM. Initially, as depicted in Figure 1b, the TEM image reveals a smooth particle surface without any noticeable $LiNbO_3$ enrichment, suggesting that the coating layer uniformly covers the NCM particles. The EDS mapping, shown in Figure 1c, identifies the presence of nickel, cobalt, manganese, oxygen and niobium elements. Furthermore, niobium exhibits high signal intensity only on the surface of NCM particles, which strongly supports the observation result of TEM shown in Figure 1b.

Next, the structure, morphology and ionic conductivity of LPSCl electrolyte were investigated through the XRD, SEM and AC impedance spectroscopy, respectively, and are shown in Supporting Information (Figure S2). In the XRD pattern of LPSCl electrolyte, a characteristic LPSCl peak was observed at 30°. Its

Research Article
doi.org/10.1002/batt.202400697
Chemistry Europe
European Chemical Societies Publishing

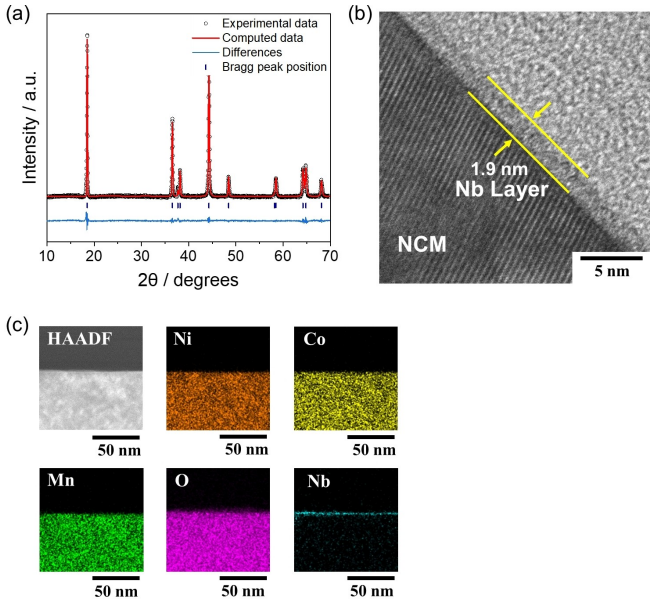

Figure 1. (a) XRD pattern with a wavelength of 1.54056 Å and Rietveld analysis result of $LiNbO_3$-coated $LiNi_{0.5}Co_{0.2}Mn_{0.3}O_2$ ($LiNbO_3$-coated NCM). The Rietveld refinement of the XRD pattern shows the material has the crystal structure of trigonal, $R\bar{3}m$ space group with a = 2.8704 Å and c = 14.2376 Å (Rwp = 2.00 %). (b) TEM image of $LiNbO_3$ coating layer on NCM. (c) EDS mapping of $LiNbO_3$-coated NCM particle.

Rietveld analysis indicates a cubic argentite structure with the space group $F\bar{4}3m$, which is consistent with the previous study.[33] The scanning electron microscopy (SEM) image of LPSCl electrolyte shows the particle size of LPSCl electrolyte is in the range of 2–20 μm. The ionic conductivity of LPSCl electrolyte at 298 K calculated by conducting AC impedance spectroscopy of LPSCl electrolyte pellet turned out to be 1.21×10^{-3} S cm^{-1}. Afterward, we investigated the morphology of composite cathode *via* X-ray CT (Figure S2d). It is confirmed that NCM and LPSCl electrolyte were uniformly distributed and the void ratio calculated by segmentation of reconstructed images was 3.53 % of total volume.

Further, the suitability of R-LTO as a reference electrode in a three-electrode cell configuration was evaluated, as illustrated in Figure S1, along with its electrochemical characteristics. The charge/discharge platform voltage of R-LTO was obtained and illustrated in Figure S3. It is evident that R-LTO maintains a stable platform voltage of 1.55 V (vs Li^+/Li) throughout the charging and discharging process. This result aligns with the results of previous studies.[34] Subsequently, as illustrated in Figure S4, we verified whether the potential and impedance of each electrode could be divided by using reference electrode R-LTO in a three-electrode cell configuration using 3 channels simultaneously. In Figure S4a, by comparing the potential between the Li-In and reference electrode, the potential of Li-In is determined to be 0.62 V (vs Li^+/Li), consistent with previous research.[35] Not only the potential of NCM cathode was successfully divided and measured for several cycles, demonstrating that the R-LTO reference electrode is suitable for dividing cathode potential from the overall cell voltage and maintaining stability throughout the subsequent cycles. When it comes to the separation of impedance, as shown in Figure S4b, the combined impedance is calculated by summing the NCM and Li-In impedances, as measured by the three-electrode configuration. When compared to the cell impedance obtained by measuring the impedance between NCM and Li-In, a significant congruence is observed. This consistency validates that R-LTO is capable of effectively separating the impedances of the NCM and Li-In, thereby establishing a robust framework for further research.

Figure S5 shows charge and discharge profiles for 3 cycles of $LiNbO_3$–coated NCM composite cathode with various cut-off potentials for charging, which are 4.0, 4.2, 4.4, 4.6, and 4.8 V (vs. Li^+/Li). Below the cut-off potential of 4.2 V (vs. Li^+/Li), there was no significant decrease in discharge capacity through cycles. On the other hand, above the cut-off potential of 4.4 V (vs. Li^+/Li), discharge capacity faded as the cycle number increased and this capacity fade intensified progressively with higher cut-off potentials. In detail, the coulombic efficiency (CE) of initial 3 cycles in $LiNbO_3$–coated NCM composite cathode with cut-off potential of 4.0 V (vs. Li^+/Li) were 79.33, 99.26, and 99.16 %, respectively. At the cut-off potential of 4.2 V (vs. Li^+/Li), CE were 84.20, 98.36 and 98.69 %, respectively. For the first cycle, irreversible capacity loss for 4.0 and 4.2 V (vs. Li^+/Li) were 28.0 and 26.5 mAh g^{-1}, respectively, which are comparable with previously reported first cycle irreversible capacity loss for NCM composite cathodes.[36,37] In contrast, for cut-off potentials equal to or greater than 4.4 V (vs. Li^+/Li), a decline in CE over the initial three cycles was quite evident. CE of initial 3 cycles of the composite cathode with cut-off potential of 4.4 V (vs. Li^+/Li) were 81.29, 95.92 and 95.42 %, respectively, while those of the composite cathode with cut-off potential of 4.6 V (vs. Li^+/Li) were 82.33, 91.51 and 94.30 %, respectively. Those two composite cathodes, cut-off potentials of 4.4 V and 4.6 V (vs. Li^+/Li), showed similar CE for the first cycle and almost similar irreversible capacity loss of 39.12 and 39.95 mAh g^{-1}, respectively. However, the composite cathode with cut-off potential of 4.6 V (vs. Li^+/Li) showed lower CE for the second and third cycles, which implies an increasing degree of irreversible changes during the charging process at elevated cut-off potentials. Finally, CE of initial 3 cycles of the composite cathode with cut-off potential of 4.8 V (vs. Li^+/Li) were 75.84, 88.81 and 93.48 %, respectively, with the first cycle irreversible capacity loss of 57.61 mAh g^{-1}. Throughout the cycling profiles of $LiNbO_3$–coated NCM composite cathode, we observed significant capacity fade above the cut-off potential of 4.4 V (vs. Li^+/Li), and this phenomenon is getting worse as cut-off potential increases, which implies an irreversible degradation happens in the cell, when charged to cut-off potential of higher than 4.4 V (vs. Li^+/Li).

In order to figure out which part of the cell is affected by the irreversible degradation that happens at high cut-off potentials, EIS analysis of $LiNbO_3$–coated NCM composite cathode under various cut-off potentials was performed as the potentials reached the cut-off potentials and carried out for 12 hours while maintaining the cut-off potentials. AC impedance measurement was conducted every hour using three-electrode cell to obtain only the impedance of cathode side.

Research Article
doi.org/10.1002/batt.202400697
Chemistry Europe
European Chemical Societies Publishing

Nyquist plots obtained from the measurement done at charging durations of 0 and 12 hours are shown in Figure 2.Firstly, as shown in Figure 2a, in the case of Nyquist plots of 0 h, as soon as the cell reached the cut-off potential, flattened and merged two semicircles and a straight line for Warburg impedance are observed, which aligns with findings from earlier research.[38] Nyquist plots obtained after maintaining various cut-off potentials for 12 hours are shown in Figure 2b. Although the complete impedance spectrum was not observed for sample with cut-off potentials higher than 4.4 V (vs. Li^+/Li) due to the limitation of frequency range, it is confirmed that the impedance of the cell increases as the cut-off potential rises. In detail, for samples with cut-off potentials higher than 4.4 V (vs. Li^+/Li), a dramatic increase in impedance was shown, while those with cut-off potentials of 4.0 V and 4.2 V (vs. Li^+/Li) showed little change. Based on these observations, it is reasonable to conclude that deterioration occurred in samples exposed to cut-off potentials higher than 4.4 V (vs. Li^+/Li), marking a distinct departure from the behavior observed at the initial two potentials. For further analysis, obtained Nyquist plots were interpreted based on equivalent circuits shown in Figure 2d. An equivalent circuit with 2 CPEs was used for Nyquist plots obtained from the samples. The two semicircles correspond to the response from the resistance of grain boundaries (R_{gb}) and that of interface between cathode material and solid electrolyte (R_{int}), respectively.[38,39] The intercept of the Z′ axis at high frequency corresponds to the bulk resistance (R_b).

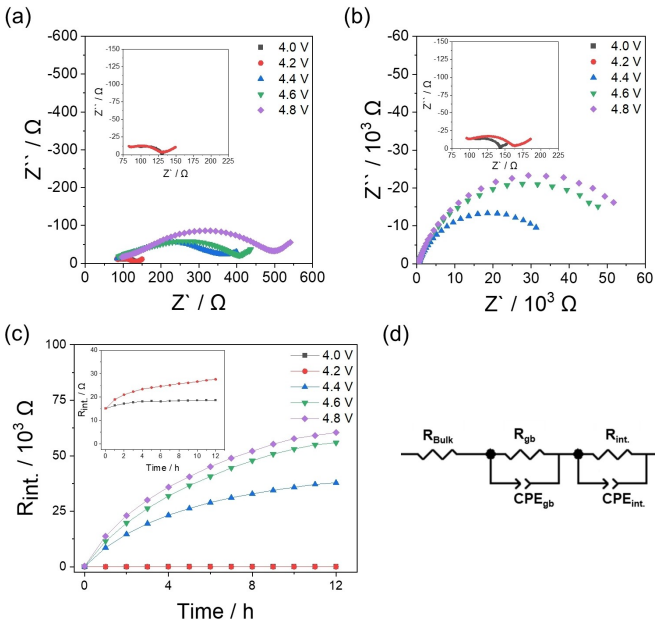

Figure 2. Nyquist plots for the impedance of $LiNbO_3$-coated NCM composite cathode using three-electrode configuration obtained (a) as soon as charged to various cut-off potentials 4.0 V, 4.2 V, 4.4 V, 4.6 V and 4.8 V (vs. Li^+/Li) at 0.1 C and (b) after maintaining each cut-off potential for 12 hours. (c) Change of interfacial resistance between cathode and solid electrolyte extracted from Nyquist plots obtained under various cut-off potentials for 12 hours after charging at 0.1 C. (d) Equivalent circuit models for $LiNbO_3$-coated NCM composite cathode. (R_{bulk} corresponds to the bulk resistance of the cell. R_{gb} reflects the resistance from the grain boundaries. $R_{int.}$ is associated with the behavior at the interface between cathode and electrolyte.)

Fitting results showed that a significant increase of impedance shown in the Nyquist plots of samples exposed to cut-off potentials higher than 4.4 V (vs. Li^+/Li) for longer than one hour mainly corresponds to R_{int}, based on the calculated capacitance value.[38,40] The temporal variations in the values of the $R_{int.}$, as determined through EIS fitting, are depicted in Figure 2c. When the cut-off potential is lower than 4.4 V (vs. Li^+/Li), the resistance slightly increases as time elapses. However, for cut-off potentials of 4.6 V (vs. Li^+/Li) or higher, the resistance increased dramatically over 12 hours. Also, the higher cut-off potential was applied, the larger $R_{int.}$ was shown. Despite the significant growth of the resistance, the growth rate of the resistance gradually slows down. These results indicate that the degradation at the interface between the composite electrode and SE occurs at different rates depending on the potential and slows down over time.

To elucidate the changes occurring in the interface between the cathode material and solid electrolyte, Nb K-edge X-ray Absorption Near Edge Structure (XANES) analysis was conducted utilizing XAS data obtained at the extremely low temperature of 10 K. Figure S6a shows the normalized Nb K-edge XANES spectra of $LiNbO_3$–coated NCM in pristine state and reference materials with possible degradation products at higher potentials.[41] Understandably, XANES spectrum of $LiNbO_3$–coated NCM in pristine state shows good agreement with that of $LiNbO_3$. However, as previously reported for XANES spectra of amorphous $LiNbO_3$ in coating layer on NCM, Nb K-edge spectrum shows a weak peak intensity due to the thin film and low quantity. Figures S6b and S6c exhibit the Nb K-edge XANES spectra of $LiNbO_3$-coated NCM composite cathode in pristine state and after being charged to various cut-off potentials for 12 hours and those in pristine state and after charged at 4.8 V (vs. Li^+/Li) for various time, respectively. The analysis of the XANES spectrum of the composite cathode samples indicates that the spectral shape largely remains constant; only subtle differences are shown among all, suggesting that detection of degradation in $LiNbO_3$ coating layer by XANES spectra is limited.

Figure S7 shows Nb K-edge EXAFS oscillations weighted by k^2 and Fourier transform EXAFS spectra of $LiNbO_3$ crystal taken at 298 K and $LiNbO_3$-coated NCM taken at 10 K and 298 K. From the spectrum obtained at 298 K, it is almost impossible to get useful information due to the high thermal disorder rather than structural disorder, which emphasizes the importance of analyzing EXAFS taken at extremely low temperature to reduces the impact of thermal disorder.[42] Fourier transform EXAFS spectra of $LiNbO_3$-coated NCM taken at 10 K show sufficient strength of the signal to analyze. Figure S7a, Nb K-edge EXAFS oscillations, exhibits that the spectrum of $LiNbO_3$-coated NCM taken at 10 K shows agreement with that of $LiNbO_3$ crystal even though it has a relatively weak signal, and this trend continues in the Fourier transform EXAFS spectra. Comparing the Fourier transform EXAFS spectrum of $LiNbO_3$ crystal and that of amorphous $LiNbO_3$ in coating layer on NCM, unlike the spectrum of $LiNbO_3$ crystal, amorphous $LiNbO_3$ shows bit broader and weaker peaks. In particular, the peak intensity at long distances is reduced, which indicates that the $LiNbO_3$ in

Research Article
doi.org/10.1002/batt.202400697
Chemistry Europe
European Chemical Societies Publishing

the coating layer is amorphous. Nevertheless, the positions of main peaks are in similar radial distances in both crystal and amorphous $LiNbO_3$, indicating that the average bond length is not largely different.

Nb K-edge Fourier transform EXAFS spectra of $LiNbO_3$-coated NCM composite cathode in pristine state and after charged to various cut-off potentials for 12 hours and those in pristine state and after charged at 4.8 V (vs. Li^+/Li) for various time are shown in Figure 3. This facilitated the acquisition of the radial distribution function for Nb atoms in $LiNbO_3$ within *R* space via Fourier transform. Peaks observed beyond a distance of 1 Å signify the presence of coordination atoms in different positions. The radial distribution in *R* space enables the direct observation of Nb's coordination atom information. Specifically, the peak position values provide a mean distance to ascertain atomic bond lengths through shell fitting, while the peak intensities reveal the number of coordinated atoms and their mean square of disorder. In comparison with the Nb K-edge Fourier transform EXAFS spectra of $LiNbO_3$-coated NCM composite cathode charged to 4.8 V (vs. Li^+/Li) for various times illustrated in Figure 3b, it is evident that the first and second proximity (about 1.13 Å and 1.81 Å, respectively) to the Nb atom consists of three oxygen atoms each. Therefore, it becomes clear that the oxygen peak in the Nb K-edge Fourier transform EXAFS spectra diminishes with increasing potential and cut-off potential keeping time, exhibiting a negative correlation with the cut-off potential and its keeping time. In other words, as the applied potential increases, the oxygen peak decreases correspondingly. For potentials over 4.4 V (vs. Li^+/Li), this reduction in the oxygen peak becomes more pronounced, aligning with the earlier EIS results, which increased resistance to increasing potential. Furthermore, for 12 hours of charge at 4.8 V (vs. Li^+/Li), the intensity of the oxygen peak in Nb coordination progressively decreased as time elapsed, displaying a negative correlation with duration. This implies that the longer the charging duration at 4.8 V, the more pronounced the reduction in the oxygen peak value becomes. However, it is noteworthy that the rate of decline in intensity of oxygen peak tends to slow down as the duration of charging is extended. These results demonstrate that the local structure of $LiNbO_3$ does change under high potential, and the oxygen desorption reaction occurs. Moreover, the degree of oxygen desorption increases as the potential increases.

The average coordination number, which denotes the mean change in coordination number among the six oxygen atoms across two bond lengths in Nb's first proximity (O2.1 and O2.2), determined by Artemis EXAFS fitting, is shown in Figure 4. The fitting results of those samples are summarized in Supporting Information (Table S1 and Table S2). Figure 4a illustrates that with increasing potential, the average oxygen coordination number in the first coordination shell of Nb atoms diminishes from the initial value of 6.17 to 5.21 at 4.8 V (vs. Li^+/Li). This trend might be attributed to the enhanced charging and delithiation states of NCM at higher potentials, which electrochemically induce oxygen desorption in $LiNbO_3$ coating material.[28] This result suggests that the contribution of the O 2p orbital to the valence band of $LiNbO_3$ is large at the density of states (DOS) and that holes are introduced into the O 2p orbital at high potentials, leading to oxygen desorption.[43] In addition, as depicted in Figure 4b, the oxygen desorption reaction of $LiNbO_3$ does not transpire abruptly but instead progresses steadily over time at 4.8 V (vs. Li^+/Li). As time increases further, the reaction rate of oxygen desorption slows down, which may be due to the effect of increasing diffusion length with time, consistent with the trend of increasing impedance shown in Figure 2.

To investigate the potential degradation of the LPSCl electrolyte under high potential, S and P K-edge XANES spectra of $LiNbO_3$-coated NCM/LPSCl composite cathode at pristine condition and after exposure to 4.2 V and 4.8 V (vs. Li^+/Li) for 12 hours were obtained. As shown in Figure 5a, from the S K-edge spectra, an increase in the intensity of peak A and a subtle rightward shift in the position of white line peaks are observed.

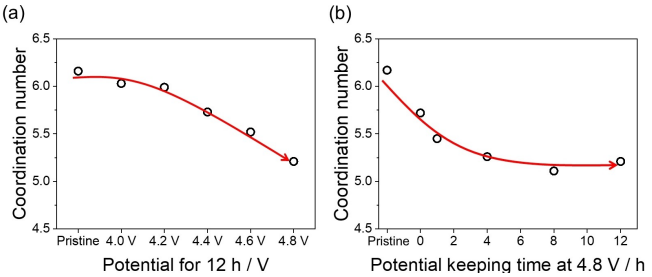

Figure 4. Correlations between the coordination number of Nb-O and (a) various cut-off potentials for 12 hours and (b) various potential keeping time at cut-off potential of 4.8 V (vs. Li^+/Li), as determined through Artemis EXAFS fitting.

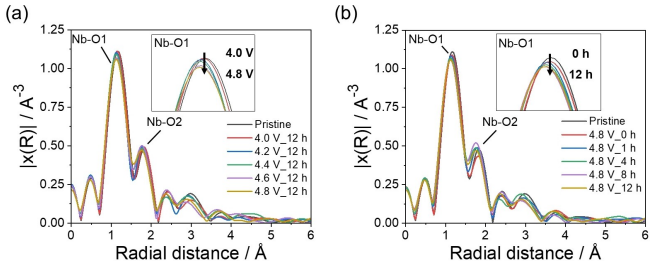

Figure 3. Nb K-edge Fourier transform EXAFS spectra of (a) $LiNbO_3$-coated NCM composite cathode charged to various cut-off potentials for 12 hours and (b) $LiNbO_3$-coated NCM composite cathode charged to 4.8 V (vs. Li^+/Li) for various time.

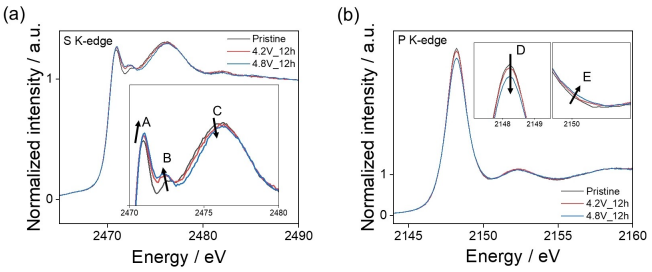

Figure 5. (a) S K-edge and (b) P K-edge XANES spectra of $LiNbO_3$-coated NCM composite cathode at pristine state and after charged to 4.2 V and 4.8 V (vs. Li^+/Li) for 12 hours.

As the potential increases, a peak designated as B becomes prominent and increases while the intensity of a peak designated as C decreases. This pattern, as indicated by previous research,[44] suggests that sulfur in the LPSCl is undergoing slight oxidation, leading to the formation of sulfur oxide groups. In the P K-edge spectra, displayed in Figure 5b, intensity of peak D was decreased while that of peak E was increased, which indicates the formation of PO_xS_y, partially oxidized PS_4^{-3} in Li6PS5Cl electrolyte.[45] In summary, these findings indicate that decomposition at the cathode interface is confined to a very thin surface layer of LPSCl.[46]

Based on the comprehensive results above, the possible degradation mechanism and reaction equation of $LiNbO_3$ coating materials are proposed, and the schematic diagram is shown in Figure 6. $LiNbO_3$ coating material undergoes an oxygen desorption side reaction, initiated by the highly charged and extensively delithiated cathode active material. This process releases oxygen, and the released oxygen reacts with the phosphorus-sulfur bonds in the LPSCl electrolyte, forming compounds such as SO_x and PO_xS_y, which exhibit extremely low ionic conductivity. These reactions contribute significantly to the considerable increase in interface resistance in the cell at high potential. According to the previous report, the thickness of the $LiNbO_3$ coating layer is critical in determining the extent of degradation. Previous reports have shown that thicker $LiNbO_3$ coatings tend to exhibit lower charge transfer resistance both initially and after cycling, suggesting enhanced protection of the underlying cathode-active material and reduced side reactions at the interface between solid electrolyte and $LiNbO_3$.[46] However, the other study also emphasizes the existence of an optimal coating thickness, beyond which the interfacial resistance can rise again.[2,5] Overall, these findings are consistent with the degradation mechanism proposed in this work, wherein oxygen desorption from the $LiNbO_3$ coating at high potentials leads to the formation of low-conductivity interfacial phases. By carefully optimizing the coating thickness, it may be possible to limit oxygen release and mitigate the ensuing degradation reactions, ultimately minimizing the rise in interfacial resistance and improving the long-term cycling stability. In addition to the equations previously outlined, the possibility of a direct reaction between the sulfide SE and the $LiNbO_3$ coating also warrants consideration. While the desorption of oxygen from the cathode active material remains a plausible scenario, the evidence suggests that the degradation of the $LiNbO_3$ coating plays a more prominent role, consistent with prior studies.[47]

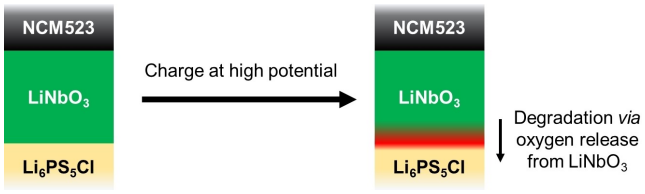

Figure 6. Schematic diagram of the possible degradation mechanism of $LiNbO_3$-coated NCM at high potential.

Conclusion

In this paper, EIS was initially employed to assess the impedance changes of the positive composite electrode maintained at various cut-off potentials for 12 hours by using three-electrode system. Through EIS fitting, we tracked the time-dependent changes in impedance components. It was observed that upon reaching a potential of 4.4 V (vs. Li^+/Li), the resistance growth rate increased significantly, indicating that the degradation reaction rate at the interface between cathode material and solid electrolyte varies with potential. Notably, degradation reactions intensify when potential goes beyond a certain threshold. Subsequent analysis using EXAFS analysis revealed that with increasing cut-off potential and potential keeping time, the coordination number of Nb–O began to decline gradually. This phenomenon is likely due to the intensified charging and delithiation states of cathode active material at elevated potentials, leading to electrochemical oxygen desorption in the $LiNbO_3$ coating material. Furthermore, it was shown that continuous exposure to high potentials gradually slows the reaction rate, which is due to an increase in the thickness of the oxygen nonstoichiometric layer in the $LiNbO_3$ layer and a decrease in the flux of oxygen by diffusion. From these results, possible degradation mechanisms and corresponding reaction equations are proposed. This discovery aims to clarify the functional mechanism and dynamic evolution of novel interfacial coating layers in ASSBs.

Acknowledgements

This work is partially based on the results obtained from a project, SOLiD-EV (JPNP18003) and SOLiD-Next (JPNP23005), subsidized by the New Energy and Industrial Technology Development Organization (NEDO). Synchrotron radiation experiments were performed at beamlines BL02B2, BL14B2, and BL20XU at SPring-8 with the approval of JASRI (proposal nos. 2022B1060, 2022B1038, 2023A1920, 2023B2029, 2024B1630).

Conflict of Interest

The authors declare no conflict of interest.

Keywords: lithium-ion battery · cathode active material · $LiNbO_3$ coating · X-ray absorption spectroscopy

[1] N. Kamaya, K. Homma, Y. Yamakawa, M. Hirayama, R. Kanno, M. Yonemura, T. Kamiyama, Y. Kato, S. Hama, K. Kawamoto, A. Mitsui, *Nat. Mater.* **2011**, *10*, 682.
[2] S. Chen, D. Xie, G. Liu, J. P. Mwizerwa, Q. Zhang, Y. Zhao, X. Xu, X. Yao, *Energy Storage Mater.* **2018**, *14*, 58.
[3] R. Murugan, V. Thangadurai, W. Weppner, *Angew. Chem. Int. Ed.* **2007**, *46*, 7778.
[4] R. Wei, S. Chen, T. Gao, W. Liu, *Nano Select* **2021**, *2*, 2256.
[5] P. Yao, H. Yu, Z. Ding, Y. Liu, J. Lu, M. Lavorgna, J. Wu, X. Liu, *Front. Chem.* **2019**, *7*, 522.
[6] P.-J. Lian, B.-S. Zhao, L.-Q. Zhang, N. Xu, M.-T. Wu, X.-P. Gao, *J. Mater. Chem. A* **2019**, *7*, 20540.

[7] K. Takada, N. Aotani, K. Iwamoto, S. Kondo, *Solid State Ion.* **1996**, *86-88*, 877.
[8] L. Xu, S. Tang, Y. Cheng, K. Wang, J. Liang, C. Liu, Y.-C. Cao, F. Wei, L. Mai, *Joule* **2018**, *2*, 1991.
[9] L. Froboese, J. F. v. d. Sichel, T. Loellhoeffel, L. Helmers, A. Kwade, *J. Electrochem. Soc.* **2019**, *166*, A318.
[10] A. Hayashi, H. Muramatsu, T. Ohtomo, S. Hama, M. Tatsumisago, *J. Mater. Chem. A* **2013**, *1*, 6320.
[11] A. Kato, M. Nose, M. Yamamoto, A. Sakuda, A. Hayashi, M. Tatsumisago, *J. Ceram. Soc. Jpn* **2018**, *126*, 719.
[12] T. K. Schwietert, V. A. Arszelewska, C. Wang, C. Yu, A. Vasileiadis, N. J. J. de Klerk, J. Hageman, T. Hupfer, I. Kerkamm, Y. Xu, E. v. d. Mass, E. M. Kelder, S. Ganapathy, M. Wagemaker, *Nat. Mater.* **2020**, *19*, 428.
[13] W. He, L. Zhou, M. K. Tufail, P. Zhai, P. Yu, R. Chen, W. Yang, *Trans. Tianjin Univ.* **2021**, *27*, 423.
[14] A. Sakuda, A. Hayashi, M. Tatsumisago, *Chem. Mater.* **2009**, *22*, 949.
[15] J. Ou, G. Li, Z. Chen, *J. Electrochem. Soc.* **2019**, *166*, A1785.
[16] C. Wang, J. Liang, S. Hwang, X. Li, Y. Zhao, K. Adair, C. Zhao, X. Li, S. Deng, X. Lin, X. Yang, R. Li, H. Huang, L. Zhang, S. Lu, D. Su, X. Sun, *Nano Energy* **2020**, *72*, 104686.
[17] S. P. Culver, R. Koerver, W. G. Zeier, J. Janek, *Adv. Energy Mater.* **2019**, *9*, 1900626.
[18] A.-Y. Kim, F. Strauss, T. Bartsch, J. H. Teo, J. Janek, T. Brezesinski, *Sci. Rep.* **2021**, *11*, 5367.
[19] H. Kitaura, A. Hayashi, K. Tadanaga, M. Tatsumisago, *Electrochim. Acta* **2010**, *55*, 8821.
[20] K. Takada, N. Ohta, L. Zhang, K. Fukuda, I. Sakaguchi, R. Ma, M. Osada, T. Sasaki, *Solid State Ion.* **2008**, *179*, 1333.
[21] A. Sakuda, H. Kitaura, A. Hayashi, K. Tadanaga, M. Tatsumisago, *J. Electrochem. Soc.* **2009**, *156*, A27.
[22] Y. Jin, N. Li, C. H. Chen, S. Q. Wei, *Electrochem. Solid-State Lett.* **2006**, *9*, A273.
[23] B. N. Nunes, W. v. d. Bergh, F. Strauss, A. Kondrakov, J. Janek, T. Brezesinski, *Inorg. Chem. Front.* **2023**, *10*, 7126.
[24] F. Walther, F. Strauss, X. Wu, B. Mogwitz, J. Hertle, J. Sann, M. Rohnke, T. Brezesinski, J. Janek, *Chem. Mater.* **2021**, *33*, 2110.
[25] N. Ohta, K. Takada, I. Sakaguchi, L. Zhang, R. Ma, K. Fukuda, M. Osada, T. Sasaki, *Electrochem. Commun.* **2007**, *9*, 1486.
[26] Y. Xiao, L. J. Miara, Y. Wang, G. Ceder, *Joule* **2019**, *3*, 1252.
[27] S. Kobayashi, H. Watanabe, T. Kato, F. Mizuno, A. Kuwabara, *ACS Appl. Mater. Interfaces* **2022**, *14*, 39459.
[28] Y. Morino, *J. Power Sources* **2022**, *541*, 231672.
[29] Y. Morino, S. Kanada, *J. Power Sources* **2021**, *509*, 230376.
[30] A. Ikezawa, G. Fukunishi, T. Okajima, F. Kitamura, K. Suzuki, M. Hirayama, R. Kanno, H. Arai, *Electrochem. Commun.* **2020**, *116*, 106743.
[31] B. Ravel, M. Newville, *J. Synchrotron Radiat.* **2005**, *12*, 537.
[32] Z. Zhong, L. Chen, S. Huang, W. Shang, L. Kong, M. Sun, L. Chen, W. Ren, *J. Mater. Sci.* **2019**, *55*, 2913.
[33] C. Yu, L. v. Eijck, S. Ganapathy, M. Wagemaker, *Electrochim. Acta* **2016**, *215*, 93.
[34] F. La Mantia, C. D. Wessells, H. D. Deshazer, Y. Cui, *Electrochem. Commun.* **2013**, *31*, 141.
[35] A. L. Santhosha, L. Medenbach, J. R. Buchheim, P. Adelhelm, *Batter. Supercaps* **2019**, *2*, 524.
[36] F. Friedrich, B. Strehle, A. T. S. Freiberg, K. Kleiner, S. J. Day, C. Erk, M. Piana, H. A. Gasteiger, *J. Electrochem. Soc.* **2019**, *166*, A3760.
[37] I. Buchberger, S. Seidlmayer, A. Pokharel, M. Piana, J. Hattendorff, P. Kudejova, R. Gilles, H. A. Gasteiger, *J. Electrochem. Soc.* **2015**, *162*, A2737.
[38] W. Zhang, D. A. Weber, H. Weigand, T. Arlt, I. Manke, D. Schroder, R. Koerver, T. Leichtweiss, P. Hartmann, W. G. Zeier, J. Janek, *ACS Appl. Mater. Interfaces* **2017**, *9*, 17835.
[39] S.-K. Jung, H. Gwon, S.-S. Lee, H. Kim, J. C. Lee, J. G. Chung, S. Y. Park, Y. Aihara, D. Im, *J. Mater. Chem. A* **2019**, *7*, 22967.
[40] J. T. S. Irvine, D. C. Sinclair, A. R. West, *Adv. Mater.* **2004**, *2*, 132.
[41] H. Chen, Z. Deng, Y. Li, P. Canepa, *Chem. Mater.* **2023**, *35*, 5657.
[42] P. Fornasini, *International Tables for Crystallography Vol. 1*, **2024**, pp. 139–146.
[43] L. Hafid, F. M. Michel-Calendini, *J. Phys. C: Solid State Phys.* **1986**, *19*, 2907.
[44] K. Sun, C. Cao, D. Zhao, X. Tong, S.-M. Bak, Y. Du, F. Wang, D. A. Steingart, *J. Phys. Chem. C* **2023**, *127*, 19396.
[45] Y. Morino, H. Tsukasaki, S. Mori, *ACS Appl. Mater. Interfaces* **2023**, *15*, 23051–23057.
[46] E. Gil-González, L. Ye, Y. Wang, Z. Shadike, Z. Xu, E. Hu, X. Li, *Energy Storage Mater.* **2022**, *45*, 484.
[47] W. S. K. Bong, A. Shiota, T. Miwa, Y. Morino, S. Kanada, K. Kawamoto, *J. Power Sources* **2023**, *577*, 233259.
[48] Y. Morino, S. Kanada, *J. Power Sources* **2021**, *509*, 230376.

Manuscript received: October 31, 2024
Revised manuscript received: January 9, 2025
Accepted manuscript online: January 22, 2025
Version of record online: February 5, 2025